



Graphitic-C₃N₄ hybridized N-doped La₂Ti₂O₇ two-dimensional layered composites as efficient visible-light-driven photocatalyst

Xiaoyan Cai ^{a,b}, Junying Zhang ^{a,*}, Mamoru Fujitsuka ^b, Tetsuro Majima ^{b,*}

^a Key Laboratory of Micro-nano Measurement, Manipulation and Physics (Ministry of Education), Department of Physics, Beihang University, Beijing, 100191, PR China

^b The Institute of Scientific and Industrial Research (SANKEN), Osaka University, Mihogaoka 8-1, Ibaraki, Osaka, 567-0047, Japan



ARTICLE INFO

Article history:

Received 2 August 2016

Received in revised form 6 September 2016

Accepted 10 September 2016

Available online 11 September 2016

Keywords:

Nitrogen doped La₂Ti₂O₇, g-C₃N₄

Layered composites

Charge transfer dynamics

ABSTRACT

Perovskite-type La₂Ti₂O₇ (LTO), having a layered structure and the separated H₂ and O₂ evolution sites, is attractive as an efficient photocatalyst. However, the photocatalytic activity is often limited by the poor electron mobility. This problem can be conquered by hybridization with materials having efficient properties for the visible light absorption and charge carrier transport. Here, we report a two-dimensional (2D) layered composite hybridized by approximately 2 nm thick graphitic C₃N₄ nanosheets (g-C₃N₄) and 7 nm thick nitrogen doped LTO nanosheets (NLTO) (g-C₃N₄/NLTO), in which g-C₃N₄ and NLTO act as hole receptor and electron conductor, respectively. g-C₃N₄/NLTO exhibited high photocatalytic activities for H₂ production via water splitting and dye degradation under the UV and visible light irradiation, due to the interfacial charge transfer between g-C₃N₄ and NLTO. The electrochemical measurement showed the type II band alignment with favorable charge transfer from g-C₃N₄ to NLTO. The 2D architecture with a maximized interfacial area allows efficient charge separation with a short interfacial distance. This efficient interfacial charge transfer is further elucidated from monitoring of charge separation and trapping processes using the femtosecond time-resolved diffused reflectance (TDR) measurement.

© 2016 Elsevier B.V. All rights reserved.

1. Introduction

Semiconductor photocatalysts have attracted considerable attention from scientists and engineers owing to their broad potential applications in solar energy conversion, medical photodynamic therapy, and environmental remediation [1]. Of the numerous photocatalysts, layer-structured semiconductors have received extensive attention owing to their layered structures which separate out the H₂ and O₂ evolution sites [2–4]. Perovskite-type photocatalysts consist of the network of corner-sharing octahedra with efficient mobility of charge carriers, showing high photocatalytic activity [5–7]. Perovskite-type La₂Ti₂O₇ (LTO) with a layered structure possesses the merits of both perovskite and layered structures to exhibit high stability and photocatalytic activity for organic decomposition, water splitting, and CO₂ reduction under the ultraviolet (UV) light irradiation [8–10]. However, the wide band gap (3.0–4.0 eV) limits the absorption spectral range within the UV light

region. In addition, the ionic character at room temperature causes the poor electron mobility and short charge carrier lifetime [11,12].

In the present paper, such problems of LTO as the photocatalyst are resolved by materials engineering to induce efficient solar energy harvesting and generation of charge carrier with longer lifetime. The recent experimental results conducted by Wu et al. demonstrated that the N-doped LTO (NLTO) nanosheets fabricated by subsequent annealing treatment in ammonia enhanced photocatalytic activity under the visible and UV irradiation [8,12,13]. Considerable reports have been focused on N-doping semiconductor thin films and powders prepared by annealing at high temperature under NH₃ flow. The N-doping method generally requires tail gas treatment and results in small amounts of N-loading (<2.5 mol%) [14–17]. Here, we present a hydrothermal method to prepare NLTO nanosheets which is simple, inexpensive, and able to produce large quantities of nanomaterials with larger amounts of N-loading (>2.5 mol%) at lower temperature (<230 °C). To our best knowledge, this is the first time to employ the hydrothermal method to dope N into layered perovskite photocatalysts. Furthermore, graphitic C₃N₄ (g-C₃N₄) was hybridized with NLTO nanosheets to further enhance the charge separation. g-C₃N₄ has high thermal and chemical stability, and has been widely studied in the field of photocatalysis in recent years [18–20]. It exhibits

* Corresponding authors.

E-mail addresses: zjy@buaa.edu.cn (J. Zhang), majima@sanken.osaka-u.ac.jp (T. Majima).

a stacking 2D layered structure, similar to that of graphite [21]. Hybridizing two kinds of 2D layered materials greatly enhances the photocatalytic activity due to increasing the interface area and interfacial charge transfer rate [22–24]. As a result, 2D layered composite hybridized by g-C₃N₄ and NLTO (g-C₃N₄/NLTO) is expected to show high photocatalytic activity.

In this study we present an approach for maximized interfacial area and shortened charge transport time and distance using ultrathin g-C₃N₄ nanosheets as a hole receptor and NLTO nanosheets as an electron conductor. This 2D heterostructure allows for simultaneously high visible light absorption and carrier collection efficiency. We also experimentally demonstrate thermodynamically favorable band alignment between NLTO and g-C₃N₄ nanosheets using electrochemical measurement. In addition, the interfacial charge transfer mechanism between NLTO and g-C₃N₄ was explored by femtosecond time-resolved diffuse reflection spectral measurement.

2. Experimental

2.1. Preparation of LTO nanosheets

LTO nanosheets were synthesized through one-step hydrothermal method as shown in Scheme S1(a). 2 mmol of La(NO₃)₃·6H₂O (Wako Pure Chemical Industries, Ltd.) and 2 mmol of Ti(SO₄)₂ (Wako, 30% aqueous) were dissolved in 10 mL Milli-Q ultrapure water (Millipore). 10 mL NaOH solution (Wako, 2 M) was dropped into the above reaction solution. After magnetically stirring for 4 h, the mixture was poured into a Teflon cup (50 mL) in a stainless autoclave and then heat at 230 °C for 24 h. After the completion of reaction, the autoclave was taken out from the incubator and left to cool-down spontaneously to room temperature. The white precipitates were collected after centrifugation, washing and drying in air at 80 °C for 12 h [8].

2.2. Preparation of NLTO

Nitrogen was doped into LTO from the hydrothermal method, followed by acid treatment to remove the byproduct (Scheme S1(b)). 0.3 g of prepared LTO white powders were added into 30 mL triethanolamine (TEOA) (Sigma-Aldrich) aqueous solution. After stirring for 1 h, the solution was put into a Teflon-lined stainless autoclave and heated at 220 °C for 48 h. The resulting solution was cooled down to room temperature. Then, it was centrifuged and washed by Milli-Q ultrapure water (Millipore) and absolute ethanol (Nacalai Tesque, Inc.) for several times. To remove the byproduct of LaCO₃OH, the obtained dark yellow precipitates were dispersed in 0.1 M HNO₃ (Wako, 69% aqueous) solution. After stirring for 30 min, the resultant bright yellow precipitates were collected after centrifugation, washing and drying in air at 80 °C for 12 h.

2.3. Preparation of g-C₃N₄ nanosheets

Bulk g-C₃N₄ was synthesized by direct heating dicyandiamide (Aldrich) at 550 °C for 4 h in static air. The resultant yellow agglomerates were milled into powder in a mortar. The light yellow powder of g-C₃N₄ nanosheets were prepared by thermal oxidation etching of bulk g-C₃N₄ obtained as above in static air as follows: 400 mg of bulk g-C₃N₄ was placed in an open ceramic container and heated at 500 °C for 2 h [20].

2.4. Preparation of g-C₃N₄/NLTO

0.3 g of as-prepared NLTO was dispersed into 20 mL Milli-Q ultrapure water (Millipore). Then, 1 mL of bulk g-C₃N₄ dispersion with different concentration was added dropwise into the N-LTO

solution under magnetic stirring to form a mixture. After stirring for 1 h and ultrasonic dispersion for 2 h, the mixture was dried in an oven at 85 °C for 12 h to evaporate the solvents. The obtained sample was ground and heated at 500 °C for 2 h (Scheme S1(c)).

2.5. Characterization

The structures of the samples were examined by X-ray diffraction (XRD, Rigaku, Smartlab; operated at 40 kV and 200 mA, Cu K α source). The morphologies were investigated using field-emission scanning electron microscopy (FESEM; JEOL, JSM-6330FT) equipped with EDX analyzer and transmission electron microscopy (TEM; JEOL, JEM3000F operated at 300 kV or Hitachi, H-800 operated at 200 kV). Chemical compositions and valence band spectra of the samples were analyzed using X-ray photoelectron spectroscopy (XPS, Shimadzu AXIS-165x). The thicknesses of the samples were measured using atomic force microscopy (AFM, Seiko Instruments Inc., SPA400). The steady-state UV-vis absorption and diffuse reflectance spectra were measured by UV-vis-NIR spectrophotometers (Jasco, V-770) at room temperature.

2.6. Photocatalytic degradation

For typical photocatalytic runs, 10 mL of g-C₃N₄/NLTO dispersion (1.0 g L⁻¹) containing methyl orange (MO, Sigma-Aldrich) aqueous solution (10 mg L⁻¹) was sonicated for 30 s. In order to reach complete adsorption/desorption equilibration, the reaction solution was stirred under dark condition for 1 h. The photocatalytic reaction was carried out by using a Xe light source (Asahi Spectra, LAX-C100; 500 mW cm⁻²) through the filters ($\lambda > 400$ nm) and a UV-LED source (Asahi Spectra, POT-365; 100 mW cm⁻²) at room temperature, respectively. During the illumination, 1 mL of the sample was centrifuged at 10 000 rpm (Hitachi, himac CF16RX) to remove the particles. The concentration of unreacted molecules was analyzed by a UV-vis spectrophotometer (Shimadzu, UV-3100) at the characteristic wavelength, from which the degradation yield was calculated.

2.7. Photocatalytic H₂ generation

2.0wt % of Pt co-catalyst was loaded on g-C₃N₄/NLTO by the photoreduction method. The photocatalyst (5 mg) was suspended in 5 mL water (Millipore) with 20 vol% methanol (Nacalai Tesque) in 30 mL glass tube. Then, the tube was sealed with a rubber septum and purged with Ar gas for 20 min before initiating the irradiation. The sample was irradiated with a Xe light source (Asahi Spectra, LAX-C100; 500 mW cm⁻²) with constant magnetic stirring at room temperature. After the reaction, 0.1 mL of gas was collected from the headspace of the reactor and analyzed using a gas chromatograph (Shimadzu GC-8A) equipped with a column and thermal conductivity detector. The apparent quantum efficiency (AQE) for H₂ evolution at each centered wavelength of the monochromatic light with width of ± 5 nm was calculated from the following equation: AQE = (2 \times number of produced H₂/number of absorbed photons) \times 100%.

2.8. Photoelectrochemical measurements

10 mg of photocatalyst powder was mixed with 20 μ L water (Millipore), 20 μ L ethanol (Nacalai Tesque) and 10 μ L nafion (Aldrich, 5wt %) under ultrasound. The formed homogenous suspension was pasted onto an ITO substrate (BAS Inc., ITO11) with doctor blading method. The pasted ITO photoelectrode was then dried on a hot plate in air. A three-electrode photoelectrochemical cell (PEC) was constructed and measured using an electrochemical

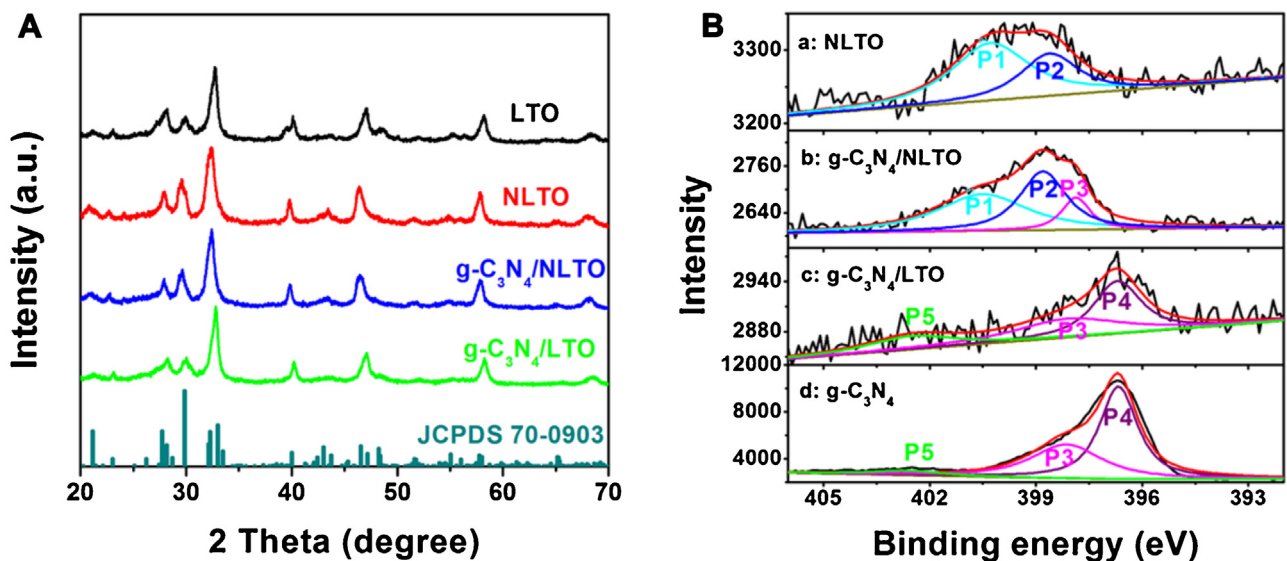


Fig. 1. X-ray diffraction patterns (A) and high-resolution XPS spectra of N 1s (B) of NLTO (a), g-C₃N₄/NLTO (10wt% g-C₃N₄) (b), g-C₃N₄/LTO (10wt% g-C₃N₄) (c), and g-C₃N₄ (d).

analyzer (ALS, model 660A). The Pt wire, Ag/AgCl, and photoelectrodes were used as the counter electrode, the reference electrode, and the working electrode, respectively. 0.1 M Na₂SO₄ aqueous solution was employed as the electrolyte (pH = 7). The plot of alternating-current impedance (EIS) was obtained under a bias of 1.23 V vs. RHE. The potential (vs. Ag/AgCl) was converted to the reversible hydrogen electrode (RHE) according to the Nernst equation: $E_{RHE} = E + 0.05916pH + E_0$, where E_{RHE} is the potential vs. RHE, $E_0 = 0.1976$ V at 25 °C, and E is the measured potential vs. Ag/AgCl.

2.9. Time-resolved diffuse reflectance spectral measurements

The femtosecond diffuse reflectance spectral measurement was performed with the pump and probe method using a regeneratively amplified titanium sapphire laser (Spectra-Physics, Spitfire Pro F, 1 kHz) pumped by a Nd:YLF laser (Spectra-Physics, Empower 15). The seed pulse was generated by a titanium sapphire laser (Spectra-Physics, Mai Tai VFSJW; fwhm 80 fs). The output (320 or 420 nm, 3 mJ pulse⁻¹) of the optical parametric amplifier (Spectra-Physics, OPA-800CF-1) was used as the excitation pulse. A white light continuum pulse, which was generated by focusing the residual of the fundamental light on a sapphire crystal after the computer controlled optical delay, was divided into two parts and used as the probe and the reference lights, of which the latter was used to compensate the laser fluctuation. Both probe and reference lights were directed to the sample powder coated on the glass substrate, and the reflected lights were detected by a linear InGaAs array detector equipped with the polychromator (Solar, MS3504). The pump pulse was chopped by the mechanical chopper synchronized to the laser repetition rate and overlapped with the probe pulse at the sample, resulting in a pair of spectra with and without the pump, from which the absorption change (% Abs) induced by the pump pulse was estimated. All measurements were carried out at room temperature.

3. Results and discussion

3.1. Characterization of g-C₃N₄/NLTO

The phase identification of the samples was performed by XRD. Fig. 1A shows XRD patterns of the pristine LTO, NLTO, NLTO loaded

with 10 wt% g-C₃N₄ (g-C₃N₄/NLTO), and LTO loaded with 10 wt% g-C₃N₄ (g-C₃N₄/LTO). All diffraction peaks of LTO and g-C₃N₄/LTO are indexed to the monoclinic phase La₂Ti₂O₇ with a perovskite structure belonging to the P21 space group (JCPDS No. 70-0903). After the hydrothermal treatment of LTO in TEOA solution, LaCO₃OH was formed accompanying with NLTO (Fig. S1a). To remove the byproduct, the obtained dark yellow precipitates were treated with diluted nitric acid. Subsequently, XRD patterns of the resultant bright yellow precipitates in Fig. 1A (pattern in red color) are assigned to pure LTO. The expansion of the crystal lattice resulted from the doping was clearly observed with the shift of the diffraction peaks toward the lower angle range, since the ion radius of N²⁻ (1.29 Å) is larger than that of O²⁻ (1.21 Å) [25,26]. For stacked g-C₃N₄ nanosheets obtained by the thermal oxidation process, the reflection peak at 12.6° in Fig. S1b corresponds to the c-plane of stacking g-C₃N₄ [27]. However, no signal assigned to g-C₃N₄ was detectable in the composites even though the percentage reaches 15 wt% (Fig. S1c and d), possibly as a result of its low crystallinity. This can also be explained by the fact that g-C₃N₄ is ultrathin and is uniformly distributed on the LTO nanosheets, as shown in the TEM and AFM images below.

The compositions of the samples were analyzed by XPS, showing that NLTO contains 5.8 at% of N after TEOA treatment (atomic concentration of La, Ti, O and N is 19.5, 27.4, 47.3 and 5.8%, respectively), which is larger than that of NLTO obtained by annealing under NH₃ flow [8]. The high chemical purity of the samples is demonstrated in Fig. S2, consisting solely of La, Ti, O, C and N. N 1s core-level XPS spectrum of NLTO in Fig. 1B-a displays two distinct peaks, N 1s peak (P1) at 400.2 eV assigned to the Ti-(N-O) bond [8,28] and N 1s peak (P2) at 398.6 eV assigned to the Ti-N bond, indicating that some N atoms are directly bonded to Ti atoms in the TiO₆ octahedron [28,29]. N 1s spectrum of g-C₃N₄ (Fig. 1B-d) confirms the existence of sp²-hybridized N (P4) at 396.7 eV, the tertiary N (N(C)₃, P3) at 398.2 eV, and the amino functional groups (P5) at 400.5 eV [30]. N 1s peaks of the composites in Figs. 1B-b and c correspond to those of their compositions, as compared with Figs. 1B-a and d. The assignment of N 1s peaks was further confirmed by the difference in the Ti 2p peaks with and without N-doping. Both LTO and g-C₃N₄/LTO exhibit symmetric Ti 2p_{3/2} peaks at 458.0 eV (Figs. S3A-a and d), which are assigned to Ti-O bond. In contrast, Ti 2p_{3/2} peaks of the NLTO are asymmetric and are deconvoluted into two

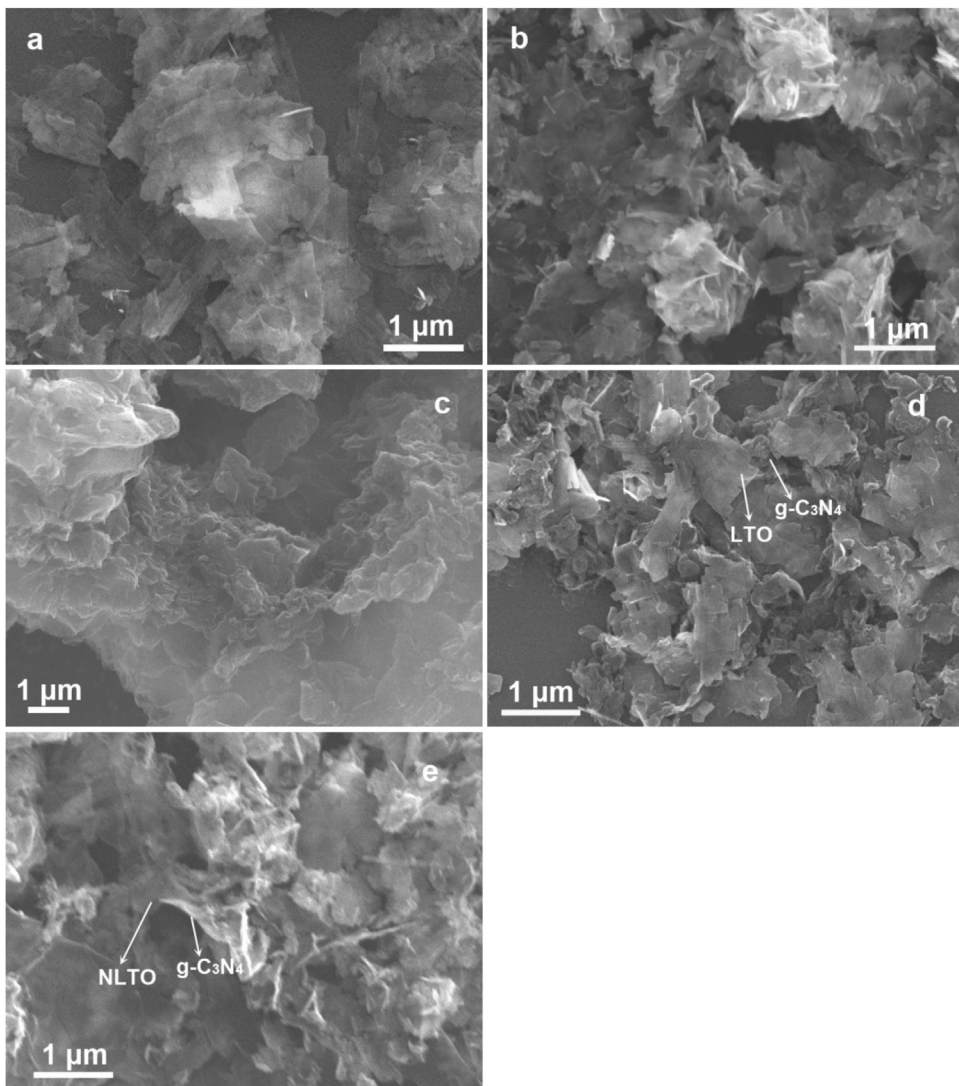


Fig. 2. SEM images of LTO (a), NLTO (b), g-C₃N₄ (c), g-C₃N₄/LTO (d), and g-C₃N₄/NLTO (e).

components (Figs. S3A-b and c). The major component is assigned to the Ti-O bond, while the peak at 458.8 eV is assigned to Ti-N bond [29]. In addition, the peaks of Ti 2p3/2 in NLTO shift to lower binding energy, indicating that the electron density around Ti in NLTO becomes higher. It can be attributed to the formation of Ti³⁺, which may cause oxygen vacancies (V_O) or interstitial Ti atoms (Ti_i) [31,32]. All four samples, LTO, NLTO, g-C₃N₄/NLTO, and g-C₃N₄/LTO, have typical O 1s spectrum with two peaks respectively located at 532.5 eV (adsorbed oxygen) and 531.0 eV (Ti-O bonds), whereas for NLTO and g-C₃N₄/NLTO, there is an additional peak at 528.6 eV which corresponds to the Ti-(N-O) bond (Figs. S3B-b and c). There is no change in the La 3d doublet peak before and after N-doping and hybridization of g-C₃N₄ (Fig. S3C), suggesting that doped N atoms are preferentially positioned in the TiO₆ octahedron slabs, in agreement with the previous studies [8,33]. C 1s spectrum derived from g-C₃N₄ (Fig. S3D) is deconvoluted into three components, C–O, C–C, and N–C=N bands [30,34,35].

The general morphologies of the materials were characterized by FESEM and TEM. Fig. 2a shows a typical SEM image of LTO, and it can be clearly seen that pure LTO is composed of smooth and irregular nanosheets with sizes ranging from 100 nm to 600 nm. N-doping does not change the sheet-like structure of LTO (Fig. 2b), which is attributed to the topochemical transformation between surface

atoms of LTO crystals suspended in a liquid phase and TEOA molecular species in solution under hydrothermal condition [36–38]. The EDS analysis in Fig. S4 exhibits La, Ti, O, and N molar ratio of 0.72: 1: 1.74: 0.2 in NLTO, consistent with the XPS analysis. The representative g-C₃N₄ nanosheets in Fig. 2c appear as loose and soft agglomerates with a size of tens of micrometers. Figs. 2d and e display the morphologies of g-C₃N₄/LTO and g-C₃N₄/NLTO, respectively. Clearly, LTO and NLTO nanosheets are irregularly dispersed on the surface of the g-C₃N₄ nanosheets. A solid construction can be achieved by such 2D/2D layered composites due to the large interface area between the sheets. Fig. 3 displays TEM and HRTEM images of LTO, NLTO, g-C₃N₄, and g-C₃N₄/NLTO. Fringes with lattice spacing of 0.28 nm in LTO and NLTO were observed clearly (inset of Figs. 3a and b), which are in accordance with (012) plane of La₂Ti₂O₇, implying a preserved crystal structure of LTO after N-doping. The appearance of a basic sheet of g-C₃N₄ in Fig. 3c is similar to that of graphite. The inserted HRTEM image demonstrates the rough surface and amorphous characterization of the g-C₃N₄ sheets. From the typical TEM image of g-C₃N₄/NLTO nanocomposites in Fig. 3d, it can be seen that NLTO nanosheets flatly lie on the surface of 2D g-C₃N₄, displaying large interfacial areas because of the 2D/2D interface between g-C₃N₄ and NLTO. Moreover, by AFM measurement, the thickness of g-C₃N₄ and NLTO are determined

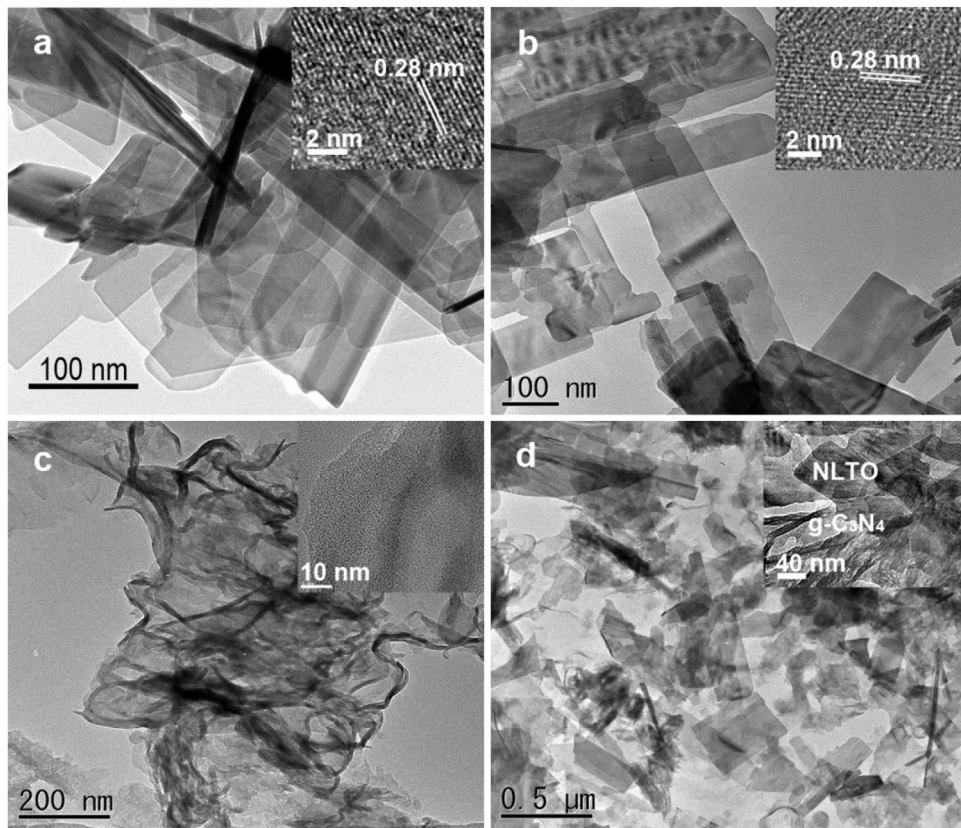


Fig. 3. TEM images of LTO (a), NLTO (b), g-C₃N₄ (c), and g-C₃N₄/NLTO (d). Insets for HRTEM images.

to be ~ 2 nm and 7 nm, respectively (Fig. S5). As the nanomaterials are thinner, the transport distance of charge carriers from photoexcited sites to reaction surface or interface becomes shorter [39]. The interfacial area in g-C₃N₄/NLTO composite system was also estimated. In Fig. S6, $\sim 83\%$ of g-C₃N₄ nanosheets are covered by NLTO nanosheets, exhibiting a large interfacial area of $0.83 \mu\text{m}^2$ per μm^2 g-C₃N₄. Hence, it is expected that the large interfacial area provides sufficient interface for efficient charge transfer, and an ultrathin heterostructure is beneficial to shorten the charge transport distance [40].

3.2. Band alignment of g-C₃N₄/NLTO

The optical responses of LTO were variable with the N doping and hybridization of g-C₃N₄, as shown in the UV-vis diffuse reflectance spectra (DRS) in Fig. 4a. Compared to pristine LTO, the absorption edges of N-doped samples (NLTO and g-C₃N₄/NLTO) show a red shift from 371 to 391 nm. Accordingly, the derived electronic band gaps from the Tauc plots are 3.17 eV for NLTO and 3.34 eV for LTO nanosheets (inset in Fig. 4a). Remarkably, add-on shoulders are imposed from 380 nm to 550 nm due to N doping

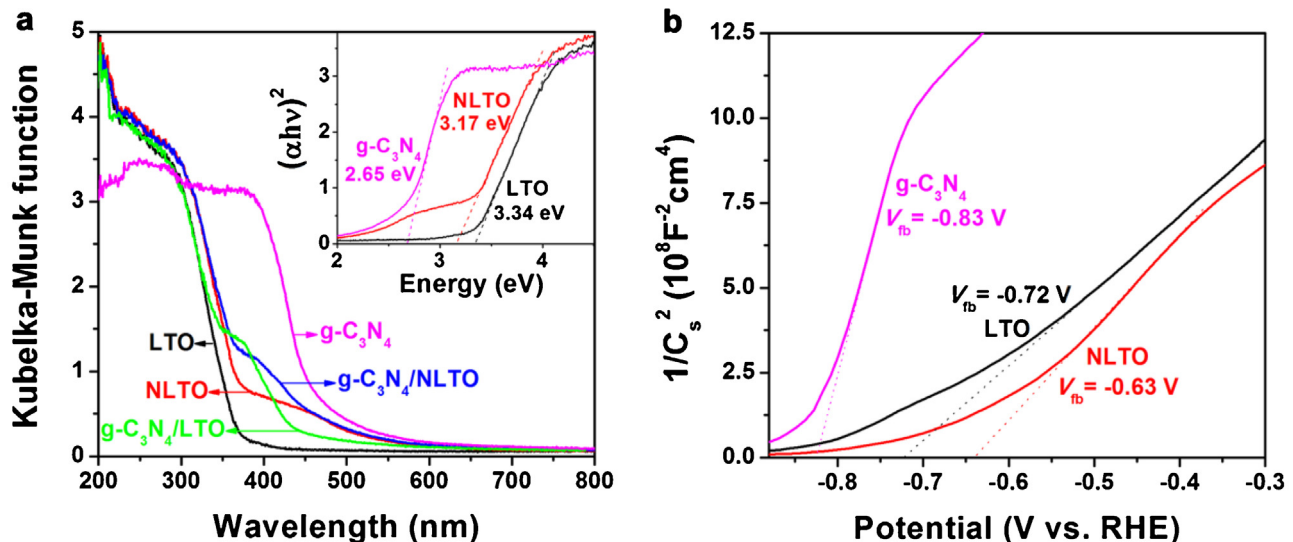


Fig. 4. (a) UV-vis diffuse reflectance spectroscopy of different samples. Inset for the optical band gap energy estimation of LTO, NLTO, and g-C₃N₄; (b) Mott-Schottky (M-S) plots of LTO, NLTO, and g-C₃N₄.

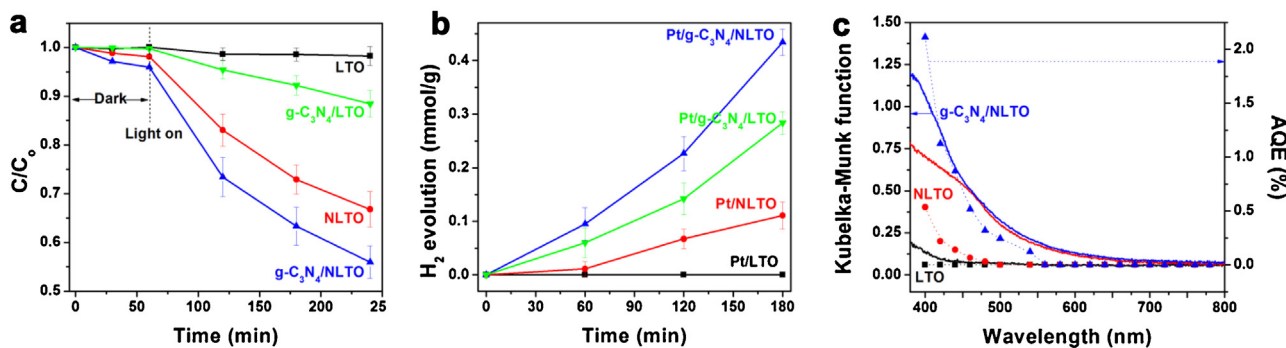


Fig. 5. Photocatalytic degradation of MO (a) and H₂ evolution (b) over different samples under the visible light irradiation. The error bars obtained through three times of repeated tests; (c) Steady-state diffuse reflectance spectra (left axis, solid lines) and AQE (right axis, symbols with dashed lines) of LTO, NLTO, and g-C₃N₄/NLTO.

with the mixed N 2p, O 2p and Ti 3d states in the midgap, as discussed below. g-C₃N₄ nanosheets exhibit the visible light response with absorption edges at 477 nm, corresponding to 2.65 eV of electronic band gap. g-C₃N₄/NLTO composite displays higher visible light harvesting ability than NLTO and g-C₃N₄/LTO due to N-doping and g-C₃N₄ modification.

Mott-Schottky measurements were analyzed to elucidate the flat-band potential V_{fb} , which are determined to be -0.72 , -0.63 , and -0.83 V vs RHE for undoped LTO, NLTO, and g-C₃N₄, respectively (Fig. 4b). The result is consistent with a type II band alignment between LTO and g-C₃N₄, since the gap between V_{fb} and bottom edge of the conduction band (CB) is assumed to be small (~ 0.2 eV) and similar for LTO and g-C₃N₄ [41]. In type II heterostructure band alignment, the position of CB and valence band (VB) of g-C₃N₄ is both higher than that of LTO. The band bending at the interface of type II heterojunction due to the difference of chemical potential between g-C₃N₄ and LTO induces a built-in field, which promotes the photoexcited electrons to facilely move from CB of g-C₃N₄ to LTO, and holes move from VB of LTO to g-C₃N₄ [42,43]. CB of the LTO nanosheets declined 0.09 eV after N-doping. Considering the 0.17 eV decrease in the bandgap and a positive shift of 0.09 eV in CB, VB of NLTO is calculated to be upshifted by 0.08 eV. We have investigated the influence of N-doping on the crystal and electronic structures of La₂Ti₂O₇ using first principles calculations [11]. Localized mid-gap states formed when N substitutions for O (N_s) co-exist with interstitial Ti atoms (Ti_i), due to the existence of Ti³⁺ (see XPS analysis). Two localized energy bands, composed of mainly Ti 3d, and the least O 2p states, covered a wide range below the conduction band minimum (CBM). Another mixed N 2p, O 2p and Ti 3d localized energy band was located 0.4 V above the valence band maximum (VBM) according to the value calculated from the density functional theory (DFT). To sum up, besides narrowing the band gap, N doping resulted in localized energy bands that cause the add-on shoulder absorption.

3.3. Photocatalytic activity of g-C₃N₄/NLTO

The photocatalytic activities of g-C₃N₄/NLTO in oxidative degradation of MO and reductive generation of H₂ were examined. Fig. 5a shows the degradation of MO in the presence of LTO, NLTO, g-C₃N₄/LTO, and g-C₃N₄/NLTO with equivalent g-C₃N₄ loadings (10 wt%), where C_0 and C are the concentrations of MO before and after the visible light irradiation, respectively. The decomposition of MO in the absence of photocatalyst or light was less than 5%, which was within the experimental tolerance range. As compared to LTO with feeble response to visible light, NLTO and/or g-C₃N₄/LTO showed markedly improvement of the oxidative efficiency. It is clearly shown that g-C₃N₄/NLTO with optimal ratio of g-C₃N₄ to NLTO exhibits the highest photocatalytic activity due

to the strongest ability of the visible light harvesting and efficient charge separation. Subsequently, a promising and synergistic improvement in the photodegradation activity was observed on g-C₃N₄/NLTO, with N-doping and hybridization of g-C₃N₄ being found to play crucial role in the degradation activity (Fig. S7). NLTO nanosheets show high photocatalytic activity under the visible and UV light irradiation. With the increase in the loading amounts of g-C₃N₄ less than 10 wt%, the degradation efficiency gradually increases with an increase of the number of photons absorbed by g-C₃N₄ nanosheets (Fig. S7b). The highest efficiency was obtained at an optimal value of 10 wt%, where approximately 44% and 95% of MO was removed under the visible and UV light irradiation within 3 h and 1 h, respectively. Similar results were observed for g-C₃N₄/LTO, except that 7.5 wt% was found to be the optimal ratio in the case of visible light irradiation (Fig. S7a).

We measured the amounts of H₂ evolved using the composites loaded with Pt as co-catalysts in aqueous solutions containing methanol as a sacrificial electron donor during the visible and simulative solar light irradiation. As shown in Fig. S8, Pt nanoparticles with size of ~ 2 nm uniformly distribute on the surface of the composite system. Under solar light irradiation (Fig. S9), N-doping significantly enhances the photocatalytic H₂ evolution rate of LTO nanosheets from 0.04 to 0.20 mmol h⁻¹ g⁻¹. The optimal g-C₃N₄/NLTO with 10 wt% g-C₃N₄ gives the H₂ evolution rate of 0.43 mmol h⁻¹ g⁻¹, which is 10 and 2 times those of LTO and NLTO, respectively. The contribution of N-doping and g-C₃N₄ modification in visible light induced activity is further examined by using a $\lambda > 400$ nm cutoff filter (Fig. 5b). The photocatalytic activity of LTO was negligibly low, while H₂ generation by NLTO, g-C₃N₄/LTO, and g-C₃N₄/NLTO was observed, confirming the visible light irradiation due to N dopants and g-C₃N₄ loading. Furthermore, the apparent quantum efficiency (AQE) at each centered wavelength of the monochromatic light was measured. The trends of H₂ evolution rates by the photocatalysts (LTO, NLTO, and g-C₃N₄/NLTO) are generally consistent with their UV/Vis DRS (Fig. 5c), indicating the photocatalytic activities are driven by the absorbed light. The photocatalytic H₂ evolution rates by the composite are always much higher than those by NLTO under the same irradiation. Under the 400-nm monochromatic light irradiation, the AQE of g-C₃N₄/NLTO (2.1%) is 4 times that of NLTO photocatalyst (0.5%). An efficient charge transfer between g-C₃N₄ and NLTO exists in the photocatalyst, which is confirmed by the femtosecond time-resolved diffuse reflection spectral measurement as described below.

3.4. Charge transfer on g-C₃N₄/NLTO

To clarify the fast interfacial charge transfer in g-C₃N₄/NLTO, we performed the EIS measurement and femtosecond TDR spectroscopy. The diameters of the arc radius on the EIS Nyquist plot

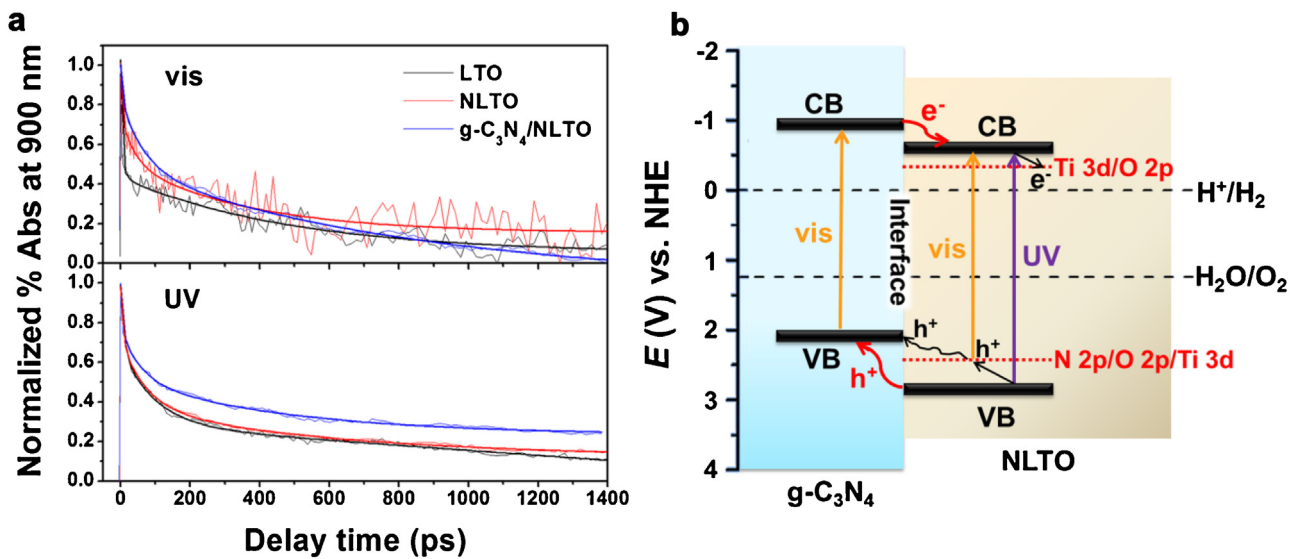


Fig. 6. (a) Normalized transient absorption trace from LTO, NLTO, and g-C₃N₄/NLTO after 420-nm or 320-nm laser irradiation; (b) Schematic illustration of the energetic distribution of electrons and holes in g-C₃N₄/NLTO under the visible (yellow arrow) and UV (purple arrow) irradiation. (For interpretation of the references to colour in this figure legend, the reader is referred to the web version of this article.)

Table 1

Kinetic parameters of decays observed for LTO, NLTO, and g-C₃N₄/NLTO under the visible or UV light irradiation.

Sample	Visible light			UV light		
	τ_1 (ps)	τ_2 (ps)	τ_3 (ps)	τ_1 (ps)	τ_2 (ps)	τ_3 (ps)
LTO	2.2 (49%)	13 (12%)	353 (39%)	5.1 (27%)	55 (34%)	463 (39%)
NLTO	2.9 (40%)	38 (37%)	864 (23%)	9.3 (31%)	74 (50%)	495 (19%)
g-C ₃ N ₄ /NLTO	5.6 (17%)	68 (35%)	496 (48%)	6.8 (31%)	96 (39%)	627 (30%)

of NLTO and/or g-C₃N₄/NLTO electrodes are smaller than that of LTO electrode (Fig. S10). The smaller the arc radius of an EIS Nyquist plot, the higher the charge separation [44]. Thus, with regard to NLTO, the electron-hole pairs are easily separated and transferred to the nanosheet surface which is due to the alteration of electronic band structure. The addition of g-C₃N₄ introduces an interfacial electron transfer from g-C₃N₄ to NLTO due to the type II band alignment.

As stated above, we have recently systematically studied the interactions between native donors and N_s in electronic band structure of NLTO [11]. Computational results suggested that when a Ti atom at an interstitial site (Ti_i) was bound with N_s, dispersely distributed localized energy states formed just above the VBM and below the CBM. The suggested mechanism associated with the results of femtosecond TDR spectroscopic measurement in Fig. 6a gives a reasonable explanation for the high photocatalytic activity of NLTO under the visible and UV light irradiation. Upon the visible light irradiation of NLTO at 420 nm, electrons are excited from mixed N 2p/O 2p/Ti 3d levels to the CB Ti 3d/O 2p to generate charge carriers (hole-electron pairs) having the broad transient absorption around 900 nm. The transient absorption decayed with three lifetimes of a few to 1000 ps (τ_1 , τ_2 , and τ_3 , Table 1). τ_1 = 2.9 ps for NLTO are greatly influenced by additional density of states (DOS) above the VB that increases relaxation of energetic carriers to the shifted band edge [45]. After charges are trapped in the localized trapping sites in the lifetime of τ_2 = 38 ps, the charge recombination occurs in the lifetime of τ_3 = 864 ps in NLTO. The hybridized localized states in NLTO (Fig. 6b) are dispersely distributed in a large energy range, even more disperse than the valence band top and conduction band bottom energy levels [11]. The charge carriers in the de-localized energy states can transport freely, unlike in the common localized energy state [46]. As a result, nitrogen doping enables the efficient

visible-light-driven photocatalytic activity of LTO. The hybridization of NLTO with g-C₃N₄ further enhances the photocatalytic degradation and H₂ production performance through generating a type II heterostructure at the maximum facet-to-facet 2D connection. The longer lifetimes of τ_1 = 5.6 ps and τ_2 = 68 ps were observed for g-C₃N₄/NLTO compared with those for NLTO, showing the similar photocatalytic activity under the UV irradiation (see below). On the other hand, the shorter lifetime of τ_3 = 496 ps was detected for g-C₃N₄/NLTO than for NLTO, indicating the fast charge transfer from CB electrons of g-C₃N₄ to CB of NLTO [39]. The time profile of the transient adsorption at 900 nm for pristine LTO under visible laser irradiation is not discussed here, because it is probably resulted from unknown impurities [36]. Under the UV laser irradiation at 320 nm, LTO showed three decay profiles with lifetimes of 5.1 ps (τ_1), 55 ps (τ_2), and 463 ps (τ_3) (Fig. 6a and Table 1). The generated electrons and holes on pristine LTO are usually trapped at the surface defects (τ_1) separately to react with water or organic molecules with substantial photocatalytic efficiency. Compared with those for LTO, decay lifetimes of 9.3 ps (τ_1), 74 ps (τ_2), and 495 ps (τ_3) were observed to show the slower charge recombination process for NLTO, due to the decreased electron-hole recombination on N 2p/O 2p/Ti 2p trap state. Thus, the efficient charge separation of NLTO was observed with the higher photocatalytic activity under the UV irradiation compared to that for LTO. g-C₃N₄/NLTO exhibited high photocatalytic activity with the longer lifetimes of charge carriers, 6.8 ps (τ_1), 96 ps (τ_2), and 627 ps (τ_3), under the same irradiation condition. The band bending at the interface of type II heterojunction due to the difference of potential energies between NLTO and g-C₃N₄ induces a built-in field (Fig. 6b), which promotes the electron-hole pair to facilely migrate to the opposite directions [41]. The large interfacial area of 2D layered g-C₃N₄/NLTO composite results in sufficient interface for efficient charge transfer

to generate an excellent type II heterojunction. The ultrathin g-C₃N₄/NLTO heterostructure (~2 nm thick g-C₃N₄ and 7 nm thick NLTO) shortens the charge transport time and distance, decreasing the recombination of photogenerated electron-hole pairs during migration.

4. Conclusions

Approximately 7 nm thick NLTO nanosheets hybridized with 2 nm thick g-C₃N₄ layered composites, g-C₃N₄/NLTO, have been synthesized from a simple two-step hydrothermal process followed by a modified thermal oxidation etching method. g-C₃N₄/NLTO was characterized by a variety of measurements and the photocatalytic activities were evaluated from H₂ production from water splitting and MO decomposition in aqueous solution. It was found that NLTO nanosheets form the interface with the surface of 2D g-C₃N₄, with the maximum interface. g-C₃N₄/NLTO exhibited a high AQE of 2.1% for photocatalytic H₂ evolution under the 400-nm monochromatic light irradiation. Such high photocatalytic activities are explained by the properties of g-C₃N₄ and NLTO, efficient light absorption and electron transport ability. Electrochemical and spectroscopic measurements were performed to clarify the type II band alignment for favorable electron transfer from g-C₃N₄ to NLTO. The long charge carrier lifetime of g-C₃N₄/NLTO measured by femtosecond time-resolved diffused reflectance (TDR) spectroscopy clearly indicates its high photocatalytic activity under the visible and UV laser irradiation. It is suggested that the large interface between 2D layered g-C₃N₄ and NLTO as well as their ultrathin heterostructure lead to efficient interfacial charge transfer to generate the charge separation with long lifetime.

Acknowledgements

This project is financially supported by the National Science Foundation of China under Grant No. 51472013, Beijing Key Discipline Foundation of Condensed Matter Physics, and China Scholarship Council (CSC). We are thankful for the help of the Comprehensive Analysis Center of SANKEI, Osaka University. This work has been partly supported by a Grant-in-Aid for Scientific Research (Project 25220806, 25288035, and others) from the Ministry of Education, Culture, Sports, Science and Technology (MEXT) of the Japanese Government.

Appendix A. Supplementary data

Supplementary data associated with this article can be found, in the online version, at <http://dx.doi.org/10.1016/j.apcatb.2016.09.021>.

References

- [1] Z. Bian, T. Tachikawa, P. Zhang, M. Fujitsuka, T. Majima, *J. Am. Chem. Soc.* 136 (2014) 458–465.
- [2] H.G. Kim, D.W. Hwang, J. Kim, Y.G. Kim, J.S. Lee, *Chem. Commun.* (1999) 1077–1078.
- [3] X.C. Wang, K. Maeda, A. Thomas, K. Takanabe, G. Xin, J.M. Carlsson, K. Domen, M. Antonietti, *Nat. Mater.* 8 (2009) 76–80.
- [4] Y. Miseki, H. Kato, A. Kudo, *Energy Environ. Sci.* 2 (2009) 306–314.
- [5] H.G. Yang, G. Liu, S.Z. Qiao, C.H. Sun, Y.G. Jin, S.C. Smith, J. Zou, H.M. Cheng, G.Q. Lu, *J. Am. Chem. Soc.* 131 (2009) 4078–4083.
- [6] J. Jiang, K. Zhao, X.Y. Xiao, L.Z. Zhang, *J. Am. Chem. Soc.* 134 (2012) 4473–4476.
- [7] H. Liu, M. Luo, J.C. Hu, T.F. Zhou, R. Chen, J.L. Li, *Appl. Catal. B* 140 (2013) 141–150.
- [8] F.K. Meng, Z.L. Hong, J. Arndt, M. Li, M.J. Zhi, F. Yang, N.Q. Wu, *Nano Res.* 5 (2012) 213–221.
- [9] S. Hu, L. Jia, B. Chi, J. Pu, L.J. Jian, *J. Power Sources* 266 (2014) 304–312.
- [10] S. Hu, M. Zhu, *ChemPlusChem* (2016), <http://dx.doi.org/10.1002/cplu.201600351>.
- [11] J. Zhang, W. Dang, Z. Ao, S.K. Cushing, N. Wu, *Phys. Chem. Chem. Phys.* 17 (2015) 8994–9000.
- [12] F. Meng, S.K. Cushing, J. Li, S. Hao, N. Wu, *ACS Catal.* 5 (2015) 1949–1955.
- [13] F. Meng, J. Li, Z. Hong, M. Zhi, A. Sakla, C. Xiang, N. Wu, *Catal. Today* 199 (2013) 48–52.
- [14] R. Asahi, T. Morikawa, T. Ohwaki, K. Aoki, Y. Taga, *Science* 293 (2001) 269–271.
- [15] C. Burda, Y.B. Luo, X.B. Chen, A.C.S. Samia, J. Stout, J.L. Gole, *Nano Lett.* 3 (2003) 1049–1051.
- [16] T. Tachikawa, Y. Takai, S. Tojo, M. Fujitsuka, H. Irie, K. Hashimoto, T. Majima, *J. Phys. Chem. B* 110 (2006) 13158–13165.
- [17] H. Irie, Y. Watanabe, K. Hashimoto, *J. Phys. Chem. B* 107 (2003) 5483–5486.
- [18] Y. Li, H. Xu, S. Ouyang, D. Lu, X. Wang, D. Wang, J. Ye, *J. Mater. Chem. A* 4 (2016) 2943–2950.
- [19] H. Yu, L. Shang, T. Bian, R. Shi, G.I.N. Waterhouse, Y. Zhao, C. Zhou, L.Z. Wu, C.H. Tung, T. Zhang, *Adv. Mater.* 28 (2016) 5080–5086.
- [20] P. Niu, L. Zhang, G. Liu, H.M. Cheng, *Adv. Funct. Mater.* 22 (2012) 4763–4770.
- [21] J. Low, S. Cao, J. Yu, S. Wageh, *Chem. Commun.* 50 (2014) 1076–1077.
- [22] Y. Hou, Z. Wen, S. Cui, X. Feng, J. Chen, *Nano Lett.* 16 (2016) 2268–2277.
- [23] Q. Xiang, J. Yu, M. Jaroniec, *J. Am. Chem. Soc.* 134 (2012) 6575–6578.
- [24] F. Meng, J. Li, S.K. Cushing, M. Zhi, N. Wu, *J. Am. Chem. Soc.* 135 (2013) 10286–10289.
- [25] I. Marozua, A. Shkabkob, M. Döbelic, T. Lippert, M. Mallepellc, C.W. Schneidera, A. Weidenkaffb, A. Wokaun, *Acta Mater.* 59 (2011) 7145–7154.
- [26] X. Cai, D. Hu, S. Deng, B. Han, Y. Wang, J. Wu, Y. Wang, *Sens. Actuators B* 198 (2014) 402–410.
- [27] Q. Tay, P. Kanhere, C.F. Ng, S. Chen, S. Chakraborty, A.C.H. Huan, T.C. Sum, R. Ahuja, Z. Chen, *Chem. Mater.* 27 (2015) 4930–4933.
- [28] A. Fujishima, X.T. Zhang, D.A. Tryk, *Surf. Sci. Rep.* 63 (2008) 515–582.
- [29] J.F. Moulder, W.F. Stickle, P.E. Sobol, K.D. Bomben, *Phys. Electron.* 1 (1995).
- [30] Q. Han, B. Wang, J. Gao, Z. Cheng, Y. Zhao, Z. Zhang, L. Qu, *ACS Nano* 10 (2016) 2745–2751.
- [31] H. Liu, F. Shen, M. Xing, J. Zhang, M. Anpo, *Catal. Lett.* 144 (2014) 1494–1498.
- [32] M. Xing, J. Zhang, F. Chen, B. Tian, *Chem. Commun.* 47 (2011) 4947–4949.
- [33] A. Kasahara, K. Nukumizu, T. Takata, J.N. Kondo, M. Hara, H. Kobayashi, K. Domen, *J. Phys. Chem. B* 107 (2003) 791–797.
- [34] Y. Kang, Y. Yang, L. Yin, X. Kang, G. Liu, H.M. Cheng, *Adv. Mater.* 27 (2015) 4572–4577.
- [35] Q. Han, C.G. Hu, F. Zhao, Z.P. Zhang, N. Chen, L.T. Qu, *J. Mater. Chem. A* 3 (2015) 4612–4619.
- [36] P. Zhang, M. Fujitsuka, T. Majima, *Appl. Catal. B* 185 (2016) 181–188.
- [37] V. Kalyani, B.S. Vasile, A. Ianculescu, M.T. Buscaglia, V. Buscaglia, P. Nanni, *Cryst. Growth Des.* 12 (2012) 4450–4456.
- [38] F. Peng, L. Cai, L. Huang, H. Yu, H. Wang, *J. Phys. Chem. Solids* 69 (2008) 1657–1664.
- [39] S. Ida, T. Ishihara, *J. Phys. Chem. Lett.* 5 (2014) 2533–2542.
- [40] Y. Ao, K. Wang, P. Wang, C. Wang, J. Hou, *RSC Adv.* 6 (2016) 48599–48609.
- [41] J. Resasco, H. Zhang, N. Kornienko, N. Becknell, H. Lee, J. Guo, A.L. Briseno, P. Yang, *ACS Cent. Sci.* 2 (2016) 80–88.
- [42] H. Li, Y. Zhou, W. Tu, J. Ye, Z. Zou, *Adv. Funct. Mater.* 25 (2015) 998–1013.
- [43] Y. Lu, D. Chu, M. Zhu, Y. Dua, P. Yang, *Phys. Chem. Chem. Phys.* 17 (2015) 17355–17361.
- [44] C. Zhai, M. Zhu, F. Pang, D. Bin, C. Lu, M.C. Goh, P. Yang, Y. Du, *ACS Appl. Mater. Interfaces* 8 (2016) 5972–5980.
- [45] B.T. Yost, S.K. Cushing, F. Meng, J. Bright, D.A. Bas, N. Wu, A.D. Bristow, *Phys. Chem. Chem. Phys.* 17 (2015) 31039–31043.
- [46] N. Umezawa, J. Ye, *Phys. Chem. Chem. Phys.* 14 (2012) 5924–5934.